



**HAL**  
open science

# Coupling spectral and Finite Element methods for 3D physic-based seismic analysis from fault to structure: Application to the Cadarache site in France

Reine Fares, David Alejandro Castro Cruz, Evelyne Foerster, Fernando  
Lopez-caballero, Filippo Gatti

## ► To cite this version:

Reine Fares, David Alejandro Castro Cruz, Evelyne Foerster, Fernando Lopez-caballero, Filippo Gatti. Coupling spectral and Finite Element methods for 3D physic-based seismic analysis from fault to structure: Application to the Cadarache site in France. Nuclear Engineering and Design, 2022, 397 (1), pp.111954. 10.1016/j.nucengdes.2022.111954 . hal-03769716

**HAL Id: hal-03769716**

**<https://hal.science/hal-03769716v1>**

Submitted on 3 Aug 2023

**HAL** is a multi-disciplinary open access archive for the deposit and dissemination of scientific research documents, whether they are published or not. The documents may come from teaching and research institutions in France or abroad, or from public or private research centers.

L'archive ouverte pluridisciplinaire **HAL**, est destinée au dépôt et à la diffusion de documents scientifiques de niveau recherche, publiés ou non, émanant des établissements d'enseignement et de recherche français ou étrangers, des laboratoires publics ou privés.

1           **Coupling Spectral and Finite Element Methods for 3D physic-based seismic analysis**  
2                           **from fault to structure: application to the Cadarache site in France**

3           Reine Fares<sup>1,2\*</sup>, David Castro Cruz<sup>3</sup>, Evelyne Foerster<sup>2</sup>, Fernando Lopez-Caballero<sup>3</sup>, Filippo Gatti<sup>3</sup>

4           <sup>1</sup> Université Paris-Saclay, CEA, Service d'Études Mécaniques et Thermiques, 91191, Gif-sur-Yvette, France.

5           <sup>2</sup> Université Paris-Saclay, CEA, Département de Modélisation des Systèmes et Structures, 91191, Gif-sur-Yvette, France.

6           <sup>3</sup> Université Paris-Saclay, CentraleSupélec, ENS Paris-Saclay, CNRS, Laboratoire de Mécanique Paris-Saclay, 91190, Gif-  
7           sur-Yvette, France.

8  
9  
10  
11   Corresponding author:

12   Reine Fares

13   Laboratoire d'Etudes Mécaniques Sismiques

14   CEA/DES/ISAS/DM2S/SEMT/EMSI

15   Address: CEA SACLAY - Bât 603, 91191 Gif Sur Yvette Cedex, France

16   Email: reine.fares@cea.fr

17   Mobile: 0033666413907

18  
19  
20  
21  
22  
23  
24  
25  
26   **Abstract**

27   This paper presents the application of a coupling strategy between the Spectral (SEM) and Finite Element (FEM)  
28   Methods to solve the soil-structure interaction (SSI) problem. The SEM-FEM coupling benefits from the mesh  
29   refinement capabilities of the FEM in modeling the structure and the near soil, with the realism of the SEM for  
30   regional scale earthquake simulations from the fault to the site. To this end, the Domain Reduction Method (DRM)  
31   introduced by (Bielak et al., 2003) is herein employed. The DRM formulation solves the problem of multi-scale  
32   earthquake simulations by subdividing the fault-to-structure problem into two simpler ones, namely: problem I-  
33   containing the structure and (hereafter solved using the FEM) and problem II- containing the fault, the regional  
34   geological and surface topography, the sedimentary basin (hereafter solved using the SEM). In this work, the  
35   coupling between the FEM code CAST3M and the SEM code SEM3D is presented, verified and compared to  
36   conventional 1D deconvolution methods for SSI analysis. A seismic simulation is performed, considering a  
37   simplified virtual nuclear reactor building, artificially positioned on the Cadarache site in South-Eastern France.  
38   The applicability of the SEM3D-CAST3M coupling is demonstrated, for SSI analysis in linear elastic regime and  
39   with a 50% reduction of the model dimensions. Moreover, the coupling captures the amplified response for the  
40   nuclear structure due to the 3D spatially variable input field and to the resulting surface wave propagation in the  
41   SEM-FEM SSI analysis.

42   **Keywords:** Nuclear reactor building; Soil-structure interaction; seismic analysis; weak coupling; Finite Element  
43   Method; Spectral Element Method.

## 44 1. INTRODUCTION

45 In recent years, a continuous effort to establish improved earthquake engineering modeling techniques has been  
46 made, in order to improve the constitutive behavior models, to characterize the geotechnical and material  
47 parameters at stake, to model the site effects and the soil-structure interaction (SSI) with efficient boundary  
48 conditions.

49 One of the largest effort aims at developing more efficient numerical tools to render the complexity of wave  
50 propagation phenomena in the Earth's crust and its interaction with the built environment. Despite being the most  
51 commonly used tool for earthquake engineering applications (e.g. Fares et al., 2019; Lysmer et al., 1975; Santisi  
52 d'Avila and Lenti, 2012), the classical Finite Element Method (FEM) is rarely used for large-scale three-  
53 dimensional (3D) seismic wave propagation analyses, due to the high number of integration points per minimum  
54 wavelength, with consequent high computation costs and high performance strategies are to be used in this case  
55 (e.g. Dupros et al., 2010). Regarding nonlinear large-scale FEM simulations, Ichimura et al., (2014) computed the  
56 seismic response of a  $2\text{km} \times 2\text{km} \times 0.1\text{km}$  domain representative of a city with 13,275 structures using 10.7  
57 billion degrees of freedom (DOF). On the contrary, methods such as the Spectral Element Method (SEM) (Faccioli  
58 et al., 1997; Komatitsch and Vilotte, 1998; Mercerat et al., 2006; Guidotti et al., 2012; Gatti et al., 2018) or the  
59 Finite Difference Method (FDM) (e.g. Boore, 1972; Virieux, 1986; Moczo et al., 2004; Maeda et al., 2017) are  
60 more popular for seismological and geophysical studies, due to their high accuracy and convenience for parallel  
61 implementation.

62 There are many possible approaches to take into account the SSI and the validity of these approaches strongly  
63 depends on the considered assumptions. Following the Niigataken-Chuetsu-Oki earthquake of July 16<sup>th</sup> 2007 in  
64 Japan, several studies investigated the applied methodologies for SSI analysis (IAEA, 2011, 2009; Wang and  
65 Rambach, 2013). Since then, efforts have been made to propose methodologies for seismic design and beyond-  
66 design bases of nuclear facilities (Coleman et al., 2013, 2016; Lo Frano et al., 2010; Van Nguyen et al., 2020).  
67 Still, at present, the site topography, soil properties, spatial heterogeneity, fault front, and geometry of sedimentary  
68 site are neglected and often considered in the signal motion proposed for the site based on nuclear norms  
69 recommendations. Hence, the influence of site effects is considered indirectly in assessing seismic ground motions  
70 at sites of interest and directly in the modeling of soil horizontally homogeneous stratigraphy. However, studies  
71 have shown that the geometry and characterization of the sedimentary basin have a crucial effect on the seismic  
72 response (Manakou et al., 2010; Raptakis et al., 2000; Semblat et al., 2005). Koufoudi et al., 2015 investigated the  
73 spatial variation of the seismic motion at the ground surface, for the same seismic event, and registered differences  
74 in recordings of 15m apart. This variation can significantly modify the internal forces induced in the structures  
75 (Santisi d'Avila et al., 2022; Sextos and Kappos, 2008). On the other hand, Wang and Feau (2017) investigated  
76 the impact of the choice of the control point for the input motion on the SSI in a fragility analysis using a reduced  
77 model. The obtained results recommend defining the input at the outcrop for conventional SSI analysis, contrary  
78 to the French nuclear authorities recommendations to define the input motion at the free field (FF) (Gupta and  
79 Lacoste, 2006).

80 In order to model the earthquake phenomenon at large scale, from the fault to the structural components, there are  
81 few examples of end-to-end simulations (McCallen et al., 2021, 2020). On site-city interaction, Lu et al. (2018)  
82 proposed a nonlinear numerical coupling in SEM. An alternative, more efficient procedure suggests a coupling  
83 method for physic-based large-scale numerical wave propagation solution. Bielak et al. (2003), proposed a domain  
84 reduction method (DRM) to reduce the large computational costs of an end-to-end simulation and to apply to an  
85 equivalent force field calculated from the solution of a simpler larger domain model to a smaller local domain.  
86 This two-step approach consists of applying a weak coupling between two models, offering a simple resolution of  
87 wave propagation from fault to structure with an acceptable computational cost (e.g. Jeremic et al., 2009; Russo  
88 et al., 2017; Abell et al., 2018; Luo et al., 2019; Zhang et al., 2020; McCallen et al., 2021; Wang et al., 2021;  
89 Korres et al., 2022). Most recently, this approach was adopted for SSI analysis by Wang et al. (2021) using  
90 potential wave formulation to create a spatially varying inclined seismic wavefield and by Zhang et al. (2020)  
91 using SEM and FEM coupling.

92 In this article, the DRM methodology for SEM-FEM coupling, to perform a SSI analysis from the fault to the  
93 structure is proposed and verified, offering easier implementation and performance compared to the strong  
94 coupling approach. The latter, on the other hand, consists in simultaneously solving and communicating the two  
95 divided problems at each time steps (Brun et al., 2021; Zuchowski et al., 2018).

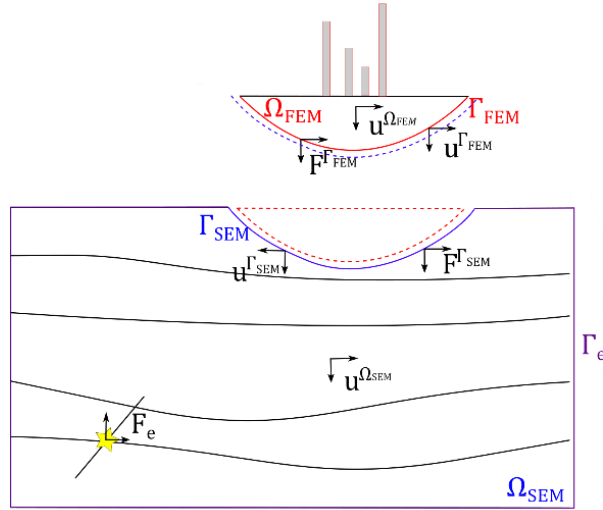
96 In the frame of the French research project SINAPS@ (Earthquake and Nuclear Installations: Ensuring and  
97 Sustaining Safety (Berge-Thierry et al., 2017), we have applied the proposed SEM-FEM coupling on the CEA  
98 (French Alternative Energies and Atomic Energy Commission) Cadarache site, located in the South-Eastern  
99 France. We have also compared the SEM-FEM coupling analysis to the Full FEM analysis for SSI (one-step

100 approach for SSI analysis using FEM Saez et al., 2011) and Free Field (FF). Finally, the choice of the input motion  
 101 implementation for the Full FEM analysis is discussed in a sensitivity study.

## 102 2. DOMAIN REDUCTION METHOD APPLIED FOR THE SEM-FEM DOMAINS COUPLING

103 The DRM method (Bielak et al., 2003) proposes a two-step analysis to solve the global problem of seismic wave  
 104 propagation from the source to the site surface, which are often several tens or even hundreds of kilometers apart.  
 105 Thus, the method divides the initial problem into two simpler ones (Figure 1). The first problem simulates the  
 106 effects of the seismic source and wave propagation with a model that includes the source and the site domain by  
 107 removing local effects, such as the site effect and the SSI ( $\Omega_{SEM}$  in Figure 1). This domain is modeled using  
 108 SEM3D, a 3D High-Performance SEM code for non-linear seismic wave propagation (CEA et al., 2017). The  
 109 second problem ( $\Omega_{FEM}$  in Figure 1) models the local site effects by considering a set of equivalent forces, derived  
 110 from the first step, and imposed on the edges of the subdomain. This domain is modeled using Cast3M, a FEM  
 111 code for structural and fluid mechanics (CEA, 2021). The discretized dynamic equilibrium equation of the wave  
 112 propagation problem in the global assembled domain  $\Omega = \Omega_{FEM} + \Omega_{SEM}$  is written in Equation (1), where  $\ddot{u}$  and  
 113  $u$  are the acceleration and displacement vectors, respectively, and  $F$  is the external loading vector. The matrices  $M$   
 114 and  $K$  represent the mass and stiffness matrices, respectively. The indices  $i$ ,  $b$  and  $e$  denote the interior, the  
 115 boundary and the exterior of the domain defined as the suffix.

$$\begin{aligned}
 & \begin{bmatrix} M_{ii}^{\Omega_{FEM}} & M_{ib}^{\Omega_{FEM}} & 0 \\ M_{bi}^{\Omega_{FEM}} & M_{bb}^{\Omega_{FEM}} + M_{bb}^{\Omega_{SEM}} & M_{be}^{\Omega_{SEM}} \\ 0 & M_{eb}^{\Omega_{SEM}} & M_{ee}^{\Omega_{SEM}} \end{bmatrix} \begin{bmatrix} \ddot{u}_i^{\Omega_{FEM}} \\ \ddot{u}_b^\Gamma \\ \ddot{u}_e^{\Omega_{SEM}} \end{bmatrix} \\
 + & \begin{bmatrix} K_{ii}^{\Omega_{FEM}} & K_{ib}^{\Omega_{FEM}} & 0 \\ K_{bi}^{\Omega_{FEM}} & K_{bb}^{\Omega_{FEM}} + K_{bb}^{\Omega_{SEM}} & K_{be}^{\Omega_{SEM}} \\ 0 & K_{eb}^{\Omega_{SEM}} & K_{ee}^{\Omega_{SEM}} \end{bmatrix} \begin{bmatrix} u_i^{\Omega_{FEM}} \\ u_b^\Gamma \\ u_e^{\Omega_{SEM}} \end{bmatrix} = \begin{bmatrix} 0 \\ 0 \\ F_e \end{bmatrix} \quad (1)
 \end{aligned}$$



116  
 117 *Figure 1. Overview of the forces and displacements applied to the boundaries of the domains  $\Omega_{SEM}$  and  $\Omega_{FEM}$ .*

118 In equation (1), the displacement is continuous at the boundaries  $\Gamma_{SEM}$  and  $\Gamma_{FEM}$  giving  $u^\Gamma = u^{\Gamma_{SEM}} = u^{\Gamma_{FEM}}$  and  
 119  $\ddot{u}^\Gamma = \ddot{u}^{\Gamma_{SEM}} = \ddot{u}^{\Gamma_{FEM}}$ . Hence,  $\Gamma$  refers to the boundaries  $\Gamma_{SEM}$  or  $\Gamma_{FEM}$ . Moreover, according to the reciprocity  
 120 theorem, the loading  $\Gamma_{FEM}$  is equal to the opposite of the forces calculated at  $\Gamma_{SEM}$   $F^{\Gamma_{FEM}} + F^{\Gamma_{SEM}} = 0$ .

121 In order to solve the wave propagation problem in  $\Omega_{FEM}$ , taking into account the effect of  $\Omega_{SEM}$ , the equivalent  
 122 force  $F_{eff}$  is calculated from the solution of the wave propagation in  $\Omega_{SEM}$  as written in Equation (2). For sake of  
 123 simplicity the full demonstration is not developed and readers are invited to refer to the paper of Bielak et al.,  
 124 (2003) for a step by step solution.

$$F_{eff} = \begin{cases} 0 \\ -M_{be}^{\Omega_{SEM}} \ddot{u}_e^{\Omega_{SEM}} - K_{be}^{\Omega_{SEM}} u_e^{\Omega_{SEM}} \\ M_{eb}^{\Omega_{SEM}} \ddot{u}_b^\Gamma + K_{eb}^{\Omega_{SEM}} u_b^\Gamma \end{cases} \quad (2)$$

125 We can summarize the proposed coupling procedures in two steps:

- 126 - The first step consists of solving the wave propagation problem in SEM3D from the fault to the free  
127 surface in  $\Omega_{SEM}$ . The corresponding model considers the soil heterogeneity in  $x$ ,  $y$  and  $z$  directions, the  
128 topography of the medium, and the fault rupture mechanism. The displacements and constraints time  
129 histories at the boundary  $\Gamma$  are logged.
- 130 - In the second step, the equivalent force  $F_{eff}$  hence calculated, according to Equation (2), is provided as  
131 input loading for the wave propagation problem in  $\Omega_{FEM}$ . The corresponding model considers the soil  
132 heterogeneous in the vertical direction  $z$  and the constructed surface to take into account the SSI effect.

133 In this paper, the proposed coupling is restrained to the linear elastic regime.

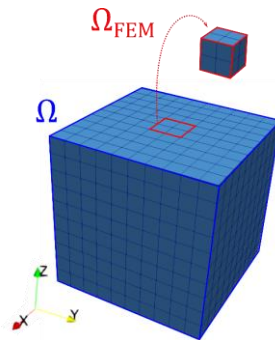
### 134 3. VERIFICATION OF THE PROPOSED SEM3D-CAST3M COUPLING

135 To be able to rely on the solution provided by the coupled computer codes, the quality of the solution needs to be  
136 evaluated. Among developers, verification and validation procedures are used to benchmark the solution with  
137 analytical or experimental outcomes (Schwer, 2009). In the field of soil dynamics, the analytical solution is not  
138 available especially for elasto-plastic or nonlinear behavior of the soil and the experimental results are hard to  
139 obtain. Hence, the V & V procedures are complicated to apply. However, there is also counter verification, where  
140 the solution is benchmarked by using the results of a verified code or from a very fine discretization. This section  
141 aims at verifying the employed procedure of coupling between both codes SEM3D and Cast3M, both validated  
142 codes in soil and structural dynamics (Gatti, 2017; Touhami et al., 2022, 2022; Wang and Rambach, 2013),

#### 143 Example 1: Counter verification of the coupling procedure with either Cast3M and SEM3D solutions

144 In order to verify the implementation of the DRM, the first example shows the comparison between a Full FEM  
145 analysis (analysis for which the solution is calculated in the domain  $\Omega$ ) using the FEM code Cast3M and a FEM-  
146 FEM analysis (the first FEM analysis solves the wave propagation in  $\Omega$  and the second one in  $\Omega_{FEM}$ , Figure 2)  
147 using the same FEM code Cast3M. A homogeneous soil with a bulk density  $\rho = 2000 \text{ kg/m}^3$ , a shear wave  
148 velocity  $v_s = 300 \text{ m/s}$  and a body wave velocity  $v_p = 700 \text{ m/s}$ , is modeled. The soil domain  $\Omega$  has larger  
149 dimensions of  $10\text{m} \times 10\text{m} \times 10\text{m}$ . The domain  $\Omega_{FEM}$  is totally embedded in the domain  $\Omega$ , with which it shares  
150 five boundary surfaces, and has a smaller dimension of  $1\text{m} \times 1\text{m} \times 1\text{m}$  (Figure 2). A Ricker-type signal is applied  
151 as a seismic input motion with a frequency equal to 5 Hz. The same time step  $\Delta t = 0.01 \text{ s}$  is adopted for Full FEM  
152 and FEM-FEM implicit analyses. When comparing the acceleration time histories registered at the center of the  
153 top ground surface for both analyses (Figure 3), a match in time and frequency domains is obtained with a  
154 difference in the peak ground acceleration (PGA) of less than 1%.

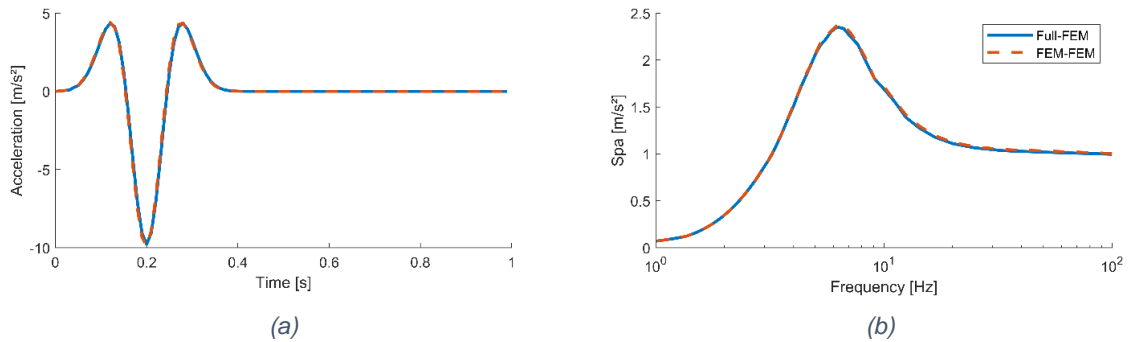
155 This same example is repeated to compare the Full SEM and the SEM-FEM coupling results. The input motion  
156 for the Full SEM model in SEM3D is a sinusoidal point source of frequency equal to 5 Hz. When comparing the  
157 acceleration time histories registered at the center of the top ground surface for both analyses (Figure 4), we obtain  
158 a difference in PGA less than 8%, which may be due to the employed interpolation at the shared surfaces nodes  
159 and the employed boundary conditions (BC). In fact, contrary to the previous Full FEM model, the Full SEM  
160 model mesh does not conform to the mesh of the reduced FEM model. In addition, the soil boundaries (lateral and  
161 at the base of the domain) damping used in Cast3M corresponds to a Lysmer-type absorbing layer (Lysmer and  
162 Kuhlemeyer, 1969; Lysmer et al., 1975), whereas the one used in SEM3D is a Perfectly Matched Layer (PML)-  
163 type absorbing layer applied (Festa and Vilotte, 2005). Finally, a Rayleigh numerical damping is used in Cast3M  
164 according to (Clough and Penzien, 2003; Hughes, 1987), with a damping matrix in the form  $C = \alpha M + \beta K$ . The  
165 Rayleigh damping is related to the inverse of the quality factor, according to the approximate relation  $Q_s = Q_p =$   
166  $v_s/10$ , such that  $Q^{-1} \approx 2\xi \approx \alpha/\omega + \beta\omega$  where  $\omega = 2\pi f$  is the pulsation and  $\xi$  the damping factor (Semblat,  
167 1997). In SEM3D on the other hand, no damping is applied.



168

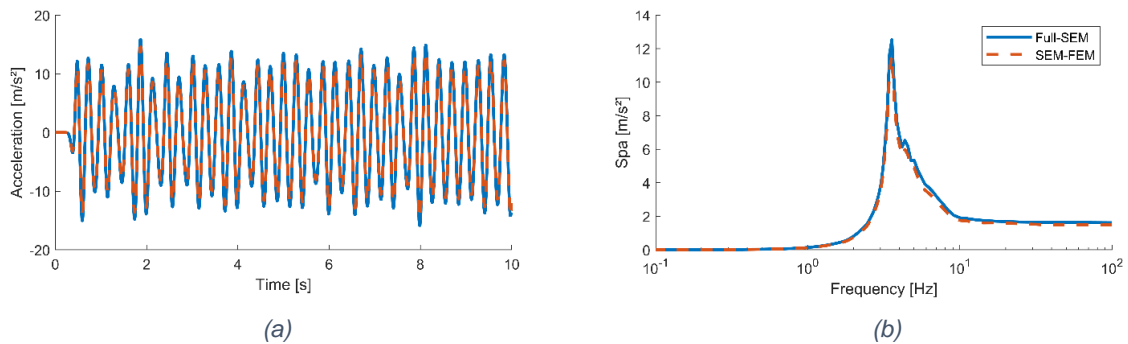
169

Figure 2 Mesh of the Full FEM domain  $\Omega$  and the reduced domain  $\Omega_{FEM}$ .



170  
171  
172  
173

Figure 3 Comparison of the time history accelerations (a) and spectral responses (b) between Full FEM and FEM-FEM coupling analyses.



174  
175  
176  
177

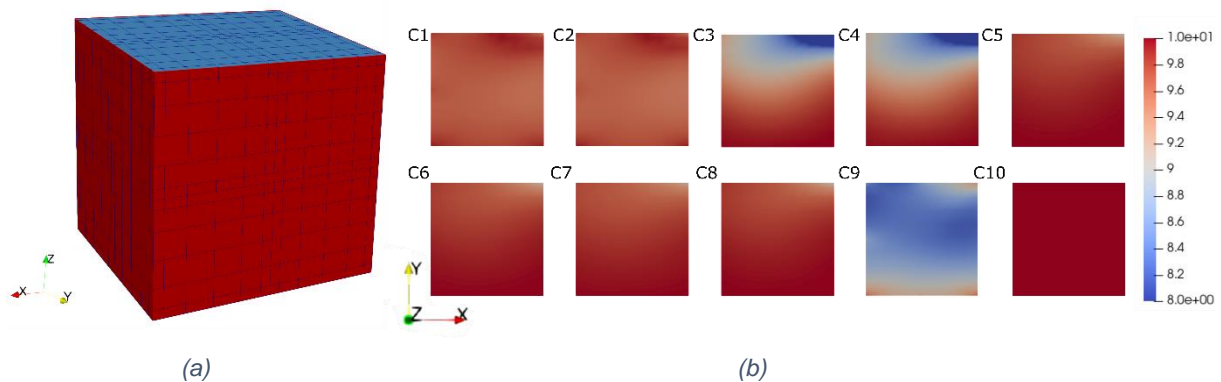
Figure 4 Comparison of the time history accelerations (a) and spectral responses (b) between Full SEM and SEM-FEM coupling analyses.

178 **Example 2: Counter verification of coupling procedure for PRENOLIN case study**

179 In order to verify the soil response solution, this example investigates the case study P1 in Régnier et al., 2016. A  
180 homogeneous soil cubic medium of  $10\text{m} \times 10\text{m} \times 10\text{m}$  is modeled with a density of  $\rho = 1800 \text{ kg/m}^3$ , a shear  
181 wave velocity of  $v_s = 300 \text{ m/s}$  and a body wave velocity of  $v_p = 700 \text{ m/s}$ . The solution is computed for a FF  
182 assumption.

183 In order to quantify the differences between the results at each node of the top ground surface for the coupling  
184 method and SEM method, Goodness of Fit (GoF) scores are calculated as proposed by Anderson, (2004). Figure  
185 5-b shows the mapping of GoF scores at the top ground surface of  $\Omega_{FEM}$ , where the results are compared according  
186 to 9 criteria with a scoring scale ranging from 0 (null fit) to 10 (excellent fit): Arias duration (C1), energy duration  
187 (C2), Arias intensity (C3), energy integral (C4), peak ground acceleration (C5), peak ground velocity (C6), peak  
188 ground displacement (C7), response spectrum (C8), Fourier spectrum (C9), over the band frequency 0.1-20Hz,  
189 and cross correlation ratio (C10). The lowest score is obtained for the Fourier spectrum  $C9 = 8.1$ , which  
190 corresponds however to an excellent fit according to Anderson, (2004). Hence, the coupling procedure is  
191 considered as verified.

192



193  
194  
195  
196

Figure 5 Mesh of the FEM model (a), mapping of the Goodness of Fit scores at the top ground surface of  $\Omega_{FEM}$  (b).

#### 197 4. APPLICATION TO THE CADARACHE SITE SIMULATION

198 The Cadarache site is a CEA center located in the South-Eastern France, with several basic nuclear facilities. It  
199 has been chosen for this study, as it is a well-instrumented site with many data on the 3D geological model,  
200 including the Middle Durance Fault, the sedimentary basin and the seismic activity. A careful seismic hazard  
201 evaluation exists for this zone due to safety requirements for the existing nuclear facilities and the proper  
202 functioning of their equipment against earthquakes.

203 In this study, the SEM3D model is used to solve the wave propagation from the fault to the free surface and to  
204 provide the displacement field at each node of the interface with the Cast3M model. In a second step, the force  
205 fields are calculated, according to the DRM (Equation (2)). The wave propagation is, hence, calculated from the  
206 near soil to the structure by solving the dynamic equilibrium equation of the assembly.

207 This procedure allows for the SSI effect while providing more accurate estimation of site effects, including the  
208 topography, the spatial variation of soil properties, and the sedimentary basin geometry, due to the variable force  
209 field loading.

210 Hereafter, we present details of the SEM3D and Cast3M models for the Cadarache site and we discuss the impact  
211 of the way to impose the input motion for the Full FEM analysis.

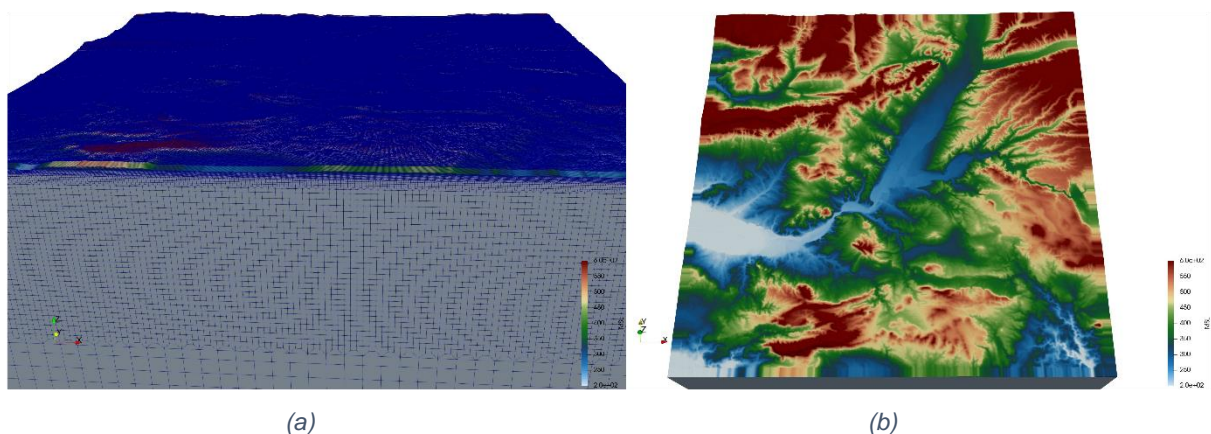
#### 212 SEM3D MODEL DESCRIPTION

213 The numerical earthquake model is implemented in SEM3D. Using the same code, Castro-Cruz et al. (2021) have  
214 proposed a hybrid approximation between a physic-based simulation and the Empirical Green function method for  
215 the Cadarache site. The study in this paper uses the same geological and source information. The model mesh for  
216 the Cadarache region contains ca. 5.9 million linear hexahedral elements for a total of 5.9 billion DOFs. PML  
217 absorbing boundary conditions are applied at the model boundaries.

218 The mesh solves with high accuracy the wave-propagation problem up to a maximum frequency of 8Hz. The  
219 elements have a minimal length of 105.8m and 45.7m inside the basin. Additionally, by using transition elements  
220 (Figure 6), with irregular hexahedrons, the elements size is larger at deeper parts where soil mechanical properties  
221 are stronger than those for the shallow layers.

222 Figure 7 presents the kinematic source introduced in the model, as a double couple mechanism by displacement  
223 imposition. This source starts around the center of the fault, and the rupture process takes around 3.8s. The  
224 maximal slip in the rupture reaches 1.1m, and the maximal released seismic moment by second is  $6 \times 10^{17} \text{ Nm/s}$ .  
225 The total seismic moment is equal to  $1.04 \times 10^{18} (M_w = 6.0)$ , which is the same magnitude as other studies in  
226 the area (e.g. Dujardin et al., 2020), and corresponds to the maximal reported magnitude in the instrument database  
227 of France (Baroux et al., 2003).

228 The Cadarache sedimentary basin model comes from the preliminary works of Guyonnet-Benaize, (2011), and has  
229 been regularly updated by the Commissariat à l'énergie atomique et aux énergies alternatives (CEA) by integrating  
230 the new data available. The basin model is constituted from thousands of boreholes investigations and numerous  
231 H/V measurements. Further details are found in Perron et al., (2018). Castro-Cruz et al. (2021) present the  
232 validation and a deeper description of the implemented geology in this model which is also used in this study. The  
233 integration between SEM and FEM allows making specific analyses on the SEM simulation. Using SEM, we  
234 predict the results at all the mesh nodes in FEM (Figure 8). The SEM model is much bigger, allowing for regional  
235 analysis, and the FEM model contributes to a more refined structural analysis.

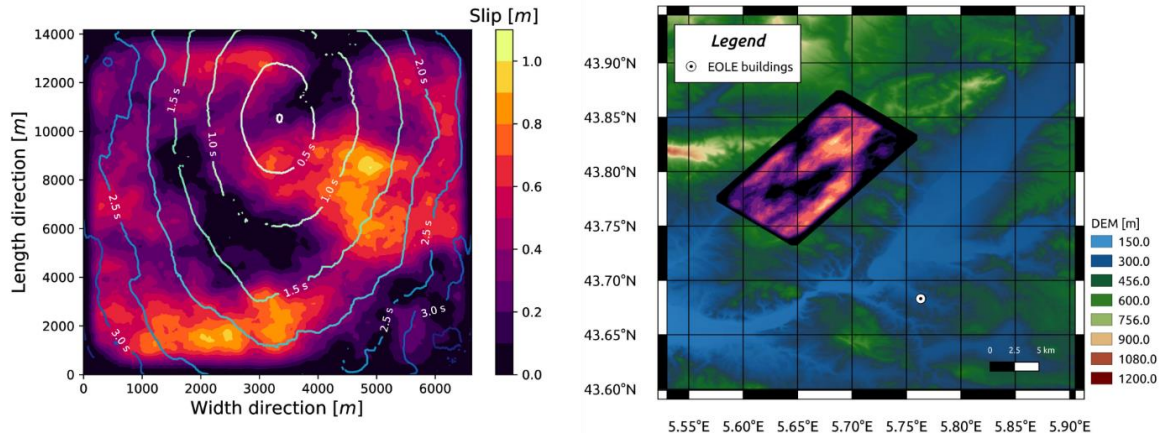


236

237

238

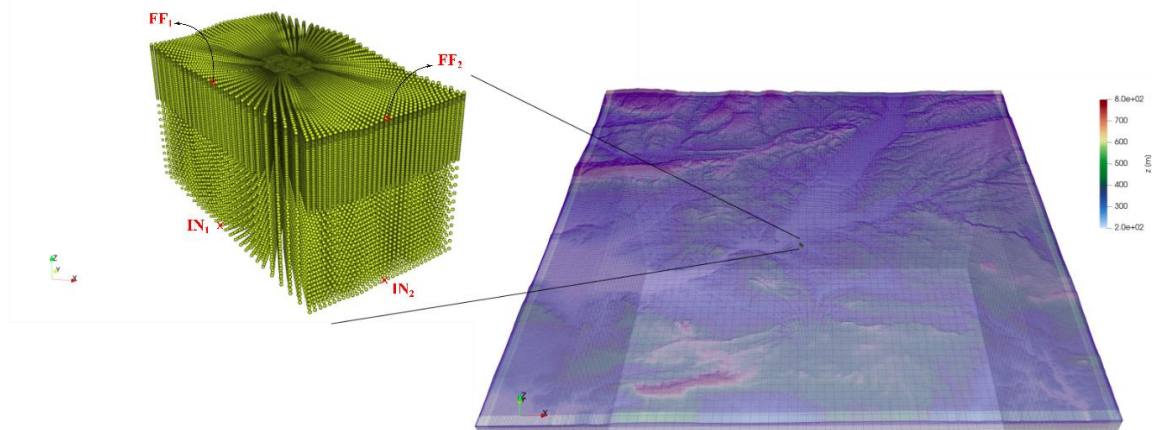
Figure 6 Mesh of the Cadarache site in SEM3D (a) and mapping of the geological model (b).



239

240 Figure 7 Seismic source for an  $M_w = 6$  earthquake, outline of the static slip distribution (a), Map of the region of  
 241 interest, including the extended fault (b).

242



243

244

Figure 8 Zoom on the receivers at which the results are predicted in the SEM3D model

## 245 CAST3M MODEL DESCRIPTION

### 246 *The soil model*

247 This study performs the coupling method using Cast3M. The soil domain modeled in Cast3M has a dimension of  
 248  $250\text{m} \times 500\text{m} \times 250\text{m}$  in  $x$ ,  $y$  and  $z$  directions respectively and is located inside the basin region (Figure 9). The  
 249 soil domain is rotated  $45^\circ$  around the  $z$  axis to match the corresponding configuration in the Cadarache site (Figure  
 250 9-a and b). The model uses a soil stratigraphy in agreement with the geological description of Cadarache site  
 251 (Appendix A), with a horizontal homogenization of the soil stratigraphy to satisfy the vertical propagation  
 252 assumption considered in the solution of the dynamic equilibrium equation in Cast3M. The adopted stratigraphy  
 253 considers thin layers of  $\Delta h \leq 5\text{ m}$  in the basin.

254 To realize SSI analysis higher frequency resolution is essential for engineering applications (Baker et al., 2014).  
 255 The objective of the study herein is to extend the resolution to frequencies relevant to structures. Moreover, higher  
 256 frequencies are observed as a result of wave scattering due to heterogeneous velocities in soil (Imperator and Mai,  
 257 2015; Takemura et al., 2015). Hence the maximum frequency of interest in this study is set to  $f = 20\text{ Hz}$ . The soil  
 258 model is meshed by hexahedral elements with quadratic interpolation for the displacement DOFs. The minimum  
 259 number of elements is defined by the analytical relation  $pfh/2v_s$ , where  $h$  is the thickness of the soil layer and  
 260  $p = 10$  is the minimum number of points per wavelength and  $v_s$  is the shear wave velocity of the soil layer (Fares,  
 261 2018). At the mesh boundaries, the model has a Lysmer-like absorbing condition to ensure the attenuation of wave  
 262 propagating towards infinity. The Newmark integration scheme is adopted for the time resolution of the dynamic  
 263 equilibrium. A Rayleigh damping model is used, to introduce frequency dependent attenuation, and is calibrated  
 264 on frequencies  $f_1 = 2\text{ Hz}$  and  $f_2 = 20\text{ Hz}$ . The damping matrix is estimated by:  $C = \alpha M + \beta K$  where  $\alpha =$   
 265  $2\zeta\omega_1\omega_2/(\omega_1 + \omega_2)$ ,  $\beta = 2\zeta/(\omega_1 + \omega_2)$  and  $\omega_1$  and  $\omega_2$  are the angular frequencies associated with the  
 266 frequencies  $f_1$  and  $f_2$  respectively. The simulations are performed in the time domain assuming linear behavior



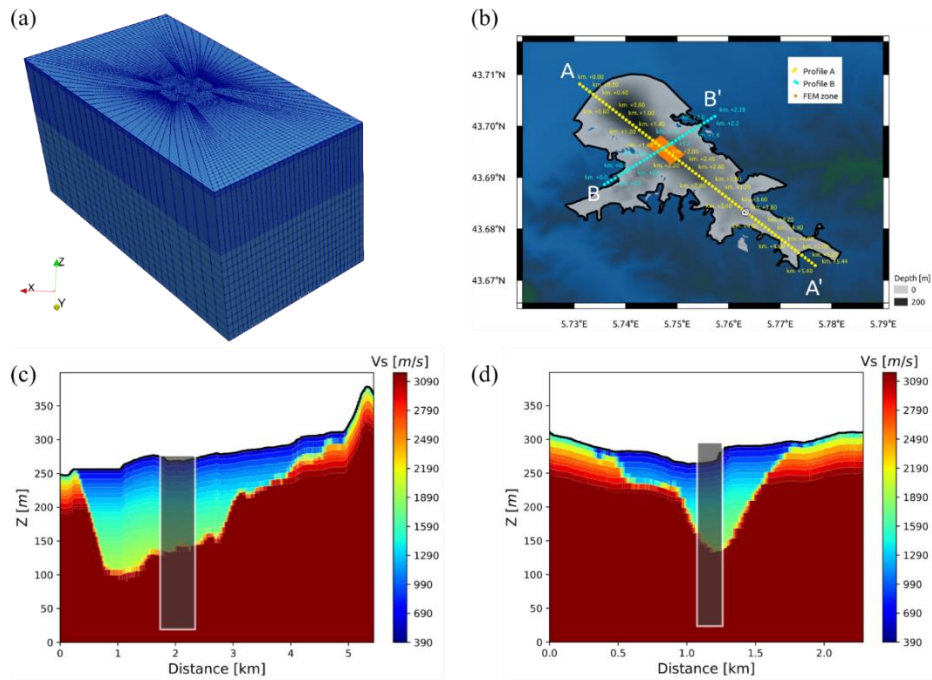


Figure 9 The soil mesh (a), the basin site (b), section AA' (c) and BB' (d) of the basin

267

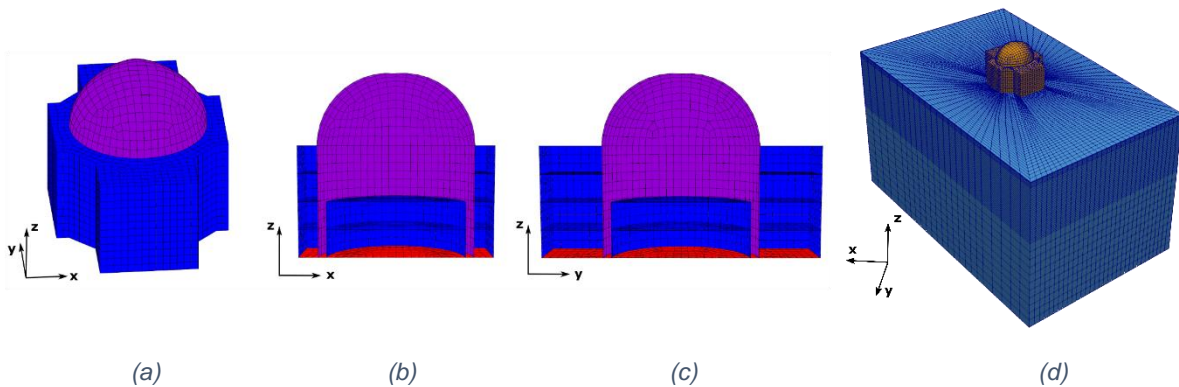
268

269 for both the structure and the soil with a time step equal to  $\Delta t = 1/(4 \times f_c) = 0.00125$  s, where  $f_c$  represents the  
 270 signal cutoff frequency.

271 *The structure model*

272 A virtual structure - corresponding to a simplified Pressurized Water Reactor (PWR)-type building - is positioned  
 273 on the Cadarache site. The used FEM model represents the detailed structure with median properties and it  
 274 incorporates all the buildings of the nuclear island, i.e. the containment, the internal structures, as well as the  
 275 backup buildings and the common basement.

276 The structure has two planes of symmetry along  $(Oxz)$  and  $(Oyz)$  (Figure 10). It is composed of a 3 m thick  
 277 foundation with dimensions  $70\text{m} \times 100\text{m} \times 65\text{m}$  and is modeled by 2D shell elements: the dome by 3-node  
 278 shell elements (COQ3), the walls and floors by 4-node shell elements (COQ4) and the invert by 8-node shell  
 279 elements (COQ8). The mechanical characteristics of the material (homogenized) composing the structure are  
 280 presented in Appendix A. The frequency of the first natural mode in bending the structure is 3.8 Hz. The  
 281 structure is connected to the ground by a rigid link at each node.



282

283

284 Figure 10 The simplified reactor building mesh: (a) 3D view, (b) plan view  $(Oxz)$  and (c) plan view  $(Oyz)$  and the  
 285 SSI model mesh (d).

286 *Investigation on input motions*

287 The choice of the input signal is critical for the accuracy of the Full FEM analysis in a nearfield domain. In the  
 288 context of SEM-FEM coupling, the method employs a spatially variable field at the reduced FEM domain  
 289 boundaries. However, in the Full FEM analysis, the method uses a uniform plane wave loading according to the

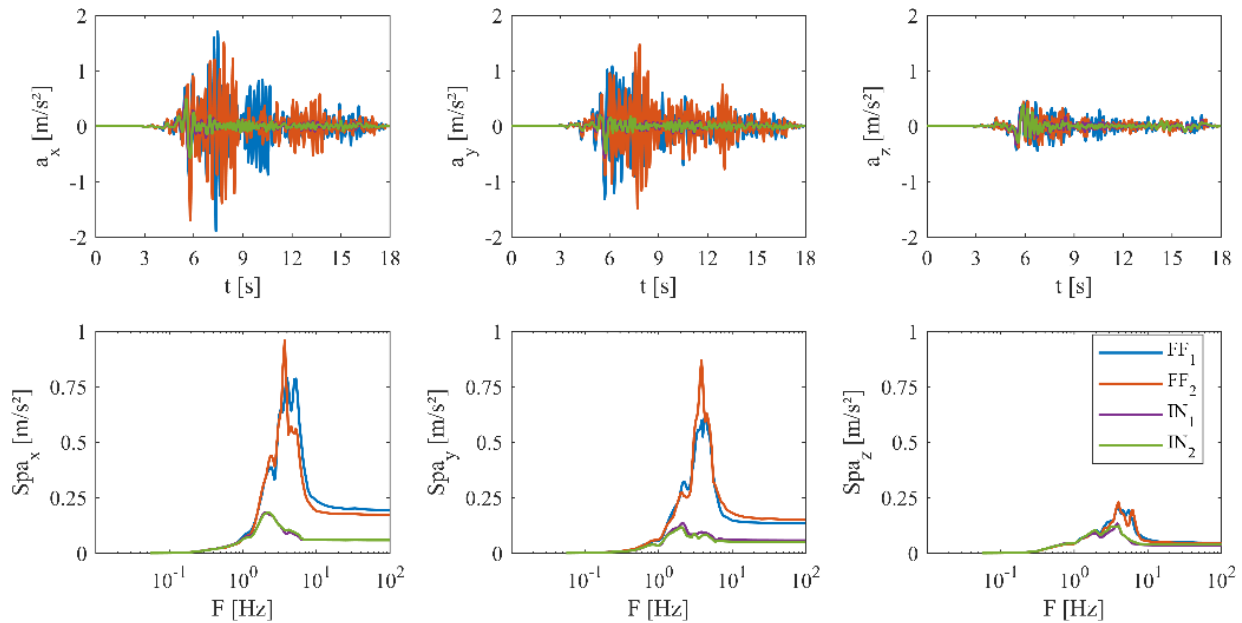
290 employed absorbing boundary condition (Lysmer and Kuhlemeyer, 1969). To generate this input field for the full  
 291 FEM analysis, we perform a deconvolution process from a FF input signal and a convolution process from an  
 292 inside bedrock (IN) input signal. The deconvolution is solved in the time domain with a transition to the frequency  
 293 domain by the computation of the transfer functions. It consists of calculating over a column soil profile the  
 294 dynamic response of each node to an impulsive horizontal input force applied at the bottom according to the  
 295 Rayleigh damping model. The convolution process is identical to the deconvolution one, but the first one predicts  
 296 the FF starting with a bedrock record and the other predicts the bedrock motion from a FF record. For simplicity,  
 297 the term deconvolution is adopted hereafter for both processes unless specified.

298 In this study, 4 different input motions are investigated: two registered at the FF ( $FF_1$  and  $FF_2$ ) and two others at  
 299 the corresponding bedrock ( $IN_1$  and  $IN_2$ ) (Figure 8 and Figure 11). Figure 12 shows a comparison between the  
 300 deconvolution and the Full SEM results in terms of normalized acceleration time histories in the soil profile for  
 301 different depths. The normalization is done according to the maximum between the maximum of absolute  
 302 accelerations  $\max|a_{z=h}^{FullSEM}|$  and  $\max|a_{z=h}^{deconvolution}|$  at each depth  $h$ . A quantification of the differences is  
 303 calculated in Table 1 computing the mean GoF coefficients at each node  $n$  in the soil profile between Full SEM  
 304 and deconvolution time history acceleration results for  $x$ ,  $y$  and  $z$  directions ( $\mu_{x,y,z}(C1) = \mu$ ). The obtained results  
 305 for the deconvolution of the FF input signals show an excellent score for all coefficients and a good score only for  
 306 the Fourier spectrum coefficient C9. However, the results obtained for the convolution of bedrock input motions  
 307 show less accuracy to reproduce the FF signal and register good results for all coefficients and very poor results  
 308 for the Arias intensity and Fourier spectrum coefficients C8 and C9 respectively. This result may be due to the  
 309 content of the FF input motions impacted by the wave propagation in the stratified soil profile. On the other hand,  
 310 the convolution of the bedrock input motions predict amplified FF signals.

311 *Table 1 Mean GoF coefficients on results at each node in the soil profile between Full SEM and deconvolution /*  
 312 *convolution time history acceleration results for  $x$ ,  $y$  and  $z$  directions.*

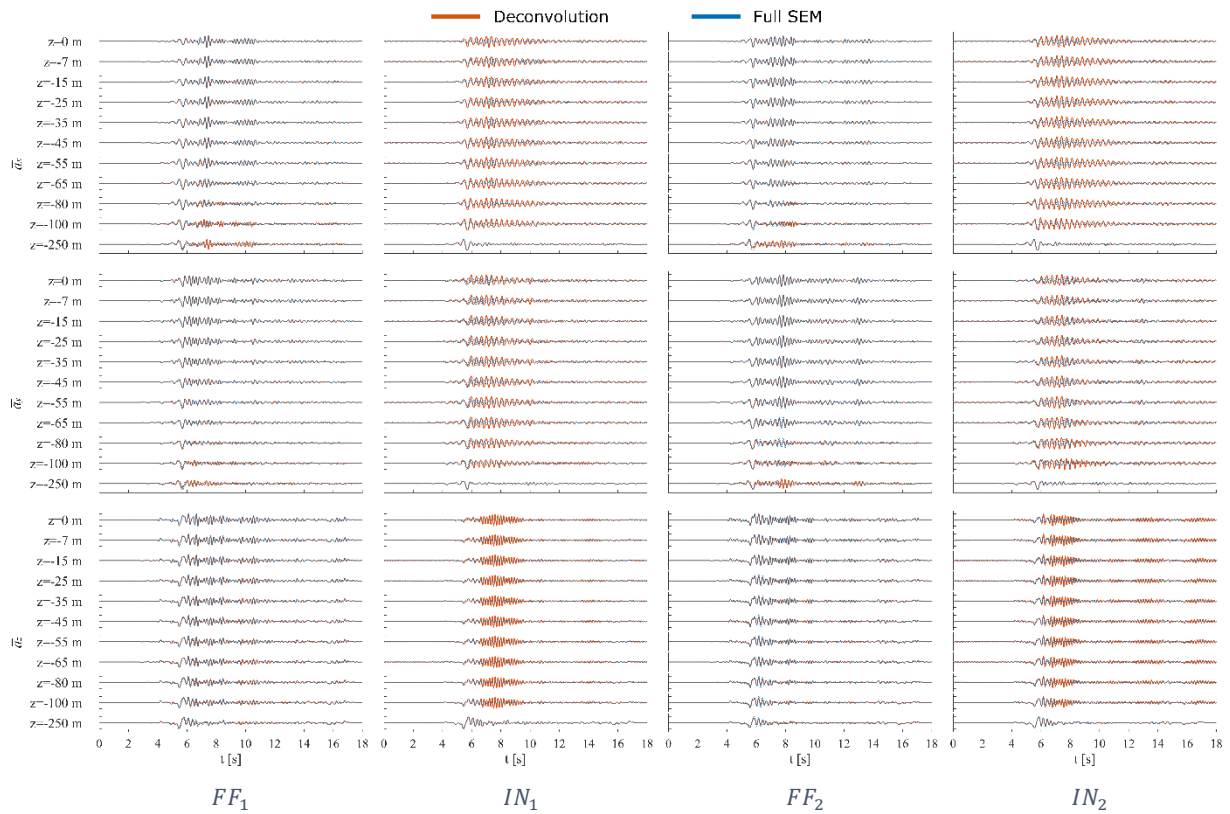
	$\mu_{x,y,z}(C1)$	$\mu_{x,y,z}(C2)$	$\mu_{x,y,z}(C3)$	$\mu_{x,y,z}(C4)$	$\mu_{x,y,z}(C5)$	$\mu_{x,y,z}(C6)$	$\mu_{x,y,z}(C7)$	$\mu_{x,y,z}(C8)$	$\mu_{x,y,z}(C9)$	$\mu_{x,y,z}(C10)$
$FF_1$	9.17	9.80	9.76	9.95	9.93	9.98	10.00	9.72	6.50	9.99
$IN_1$	7.15	7.09	0.47	3.80	5.90	9.25	7.08	6.09	0.43	9.15
$FF_2$	9.14	9.73	9.06	9.91	9.67	9.97	10.00	9.50	5.66	9.99
$IN_2$	7.45	7.48	0.77	4.50	7.65	9.58	5.54	7.45	0.43	9.44

313



314

315 *Figure 11 Time history accelerations of the studied input signals (top) and their corresponding spectral responses*  
 316 *(bottom) in  $x$ ,  $y$  and  $z$  directions.*

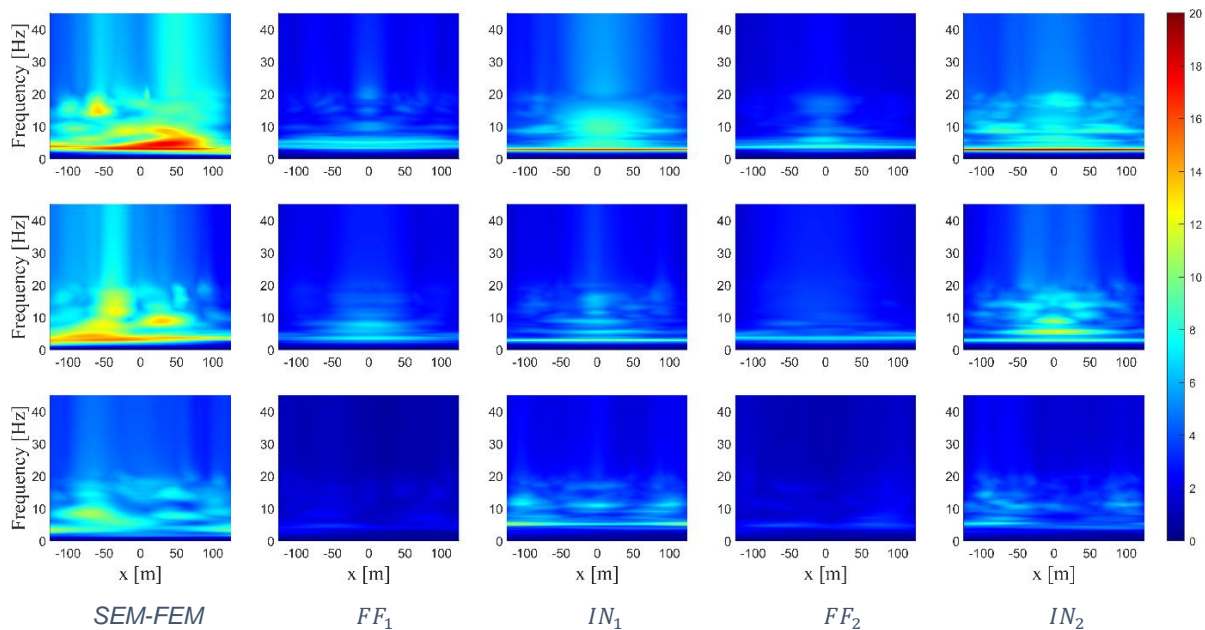


317  
318

319 *Figure 12 Comparison of the normalized time history accelerations along the soil profile depths for the Full SEM*  
320 *and the deconvolution / convolution results in x, y and z direction from top to bottom respectively.*

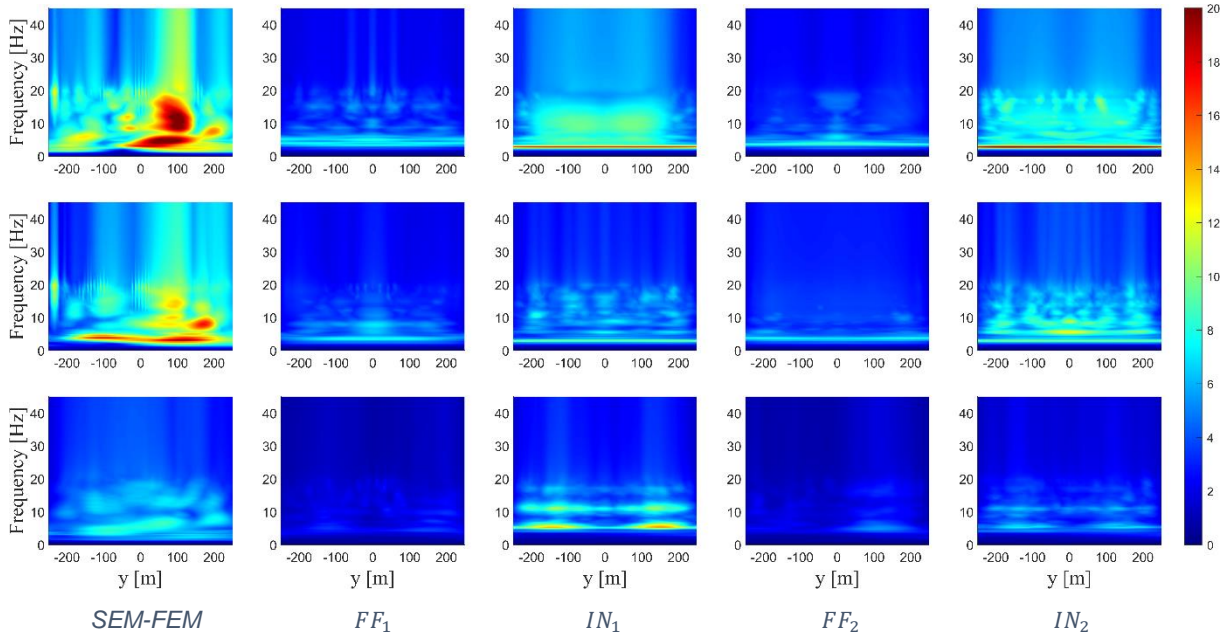
321 **FREE FIELD ANALYSIS**

322 This section presents the study of the choice in the input signal considering the site effects related to the  
323 topography, the spatial heterogeneity of the mechanical properties of the soil, and the surface waves. For this  
324 purpose, the Cadarache site is modeled in a 3D soil domain, as described previously. Contrary to the deconvolution  
325 procedure, the Full FEM and SEM-FEM analyses solve the dynamic equilibrium equation for the wave  
326 propagation in the 3D soil domain. Figure 13 and Figure 14 show a comparison between the mappings of the  
327 spectral responses of the soil surface along with the free surface lines AA' and BB' respectively (Appendix B,  
328 Figure B-1) for the SEM-FEM, and Full FEM analyses considering the input motions  $FF_1, IN_1, FF_2$  and  $IN_2$ .



329  
330  
331  
332

331 *Figure 13 Mapping of the spectral responses of the soil surface along the free surface lines AA' for the SEM-FEM*  
332 *coupling and Full FEM analyses considering the input motions  $F_1, IN_1, FF_2$  and  $IN_2$ .*



333

334

335

336

Figure 14 Mapping of the spectral responses of the soil surface along the free surface lines  $BB'$  for the SEM-FEM coupling and Full FEM analyses considering the input motions  $FF_1, IN_1, FF_2$  and  $IN_2$ .

337

338

339

340

341

342

343

The Full FEM analysis results underestimate the soil response, compared to SEM-FEM analysis. In fact, the SEM-FEM analysis allows the surface wave propagation due to the spatially variable input field. Hence, it allows a better estimation of the site effects in the soil. Although the FF input signals lead to satisfying results for the deconvolution analysis, in a Full FEM 3D wave propagation approach, the bedrock input signals perform better. According to the results obtained for input motions  $IN_1$  and  $IN_2$  in Figure 13 and Figure 14, the predominant frequency and its associated amplification correspond to the solution in SEM-FEM coupling. Whereas results obtained for input motions  $FF_1$  and  $FF_2$  show a slightly higher frequency with an attenuated energy.

344

#### SOIL-STRUCTURE INTERACTION

345

346

347

348

349

350

Modeling the wave propagation in a Full FEM 3D domain of reasonable size requires introducing boundary conditions chosen with care. This attention allows the reproduction of the diffracted wave field at infinity and limits the parasitic edge reflections (Snell's law) that can strongly degrade the solution. This is why it is not possible to consider Dirichlet type boundary conditions (i.e. imposed displacements), unless the boundary is moved away considerably, at the cost of significantly increased computation time and memory consumption, due to the increase in the size of the mesh and the number of associated DOFs.

351

352

353

354

355

356

357

358

In the case of SSI, it is preferable to use an absorbing boundary condition, which allows reproducing the far field solution (Hudson et al., 1994). Nevertheless, this type of boundary generally requires the structure to be moved away from the boundaries (lateral and at the base of the domain), in order to ensure a normal incidence of the waves at the edges, otherwise, the absorption conditions will be strongly degraded. Thus, the condition proposed by Lysmer and Kuhlemeyer (1969) pioneers in the study of the SSI, requires, for example, to move the boundaries away from the structure by a distance of  $5 \times r$  from the center of its foundation, where  $r$  represents the radius of the equivalent circular foundation. All these limitations and conditions do not apply in the case of a SEM-FEM calculation.

359

360

361

362

363

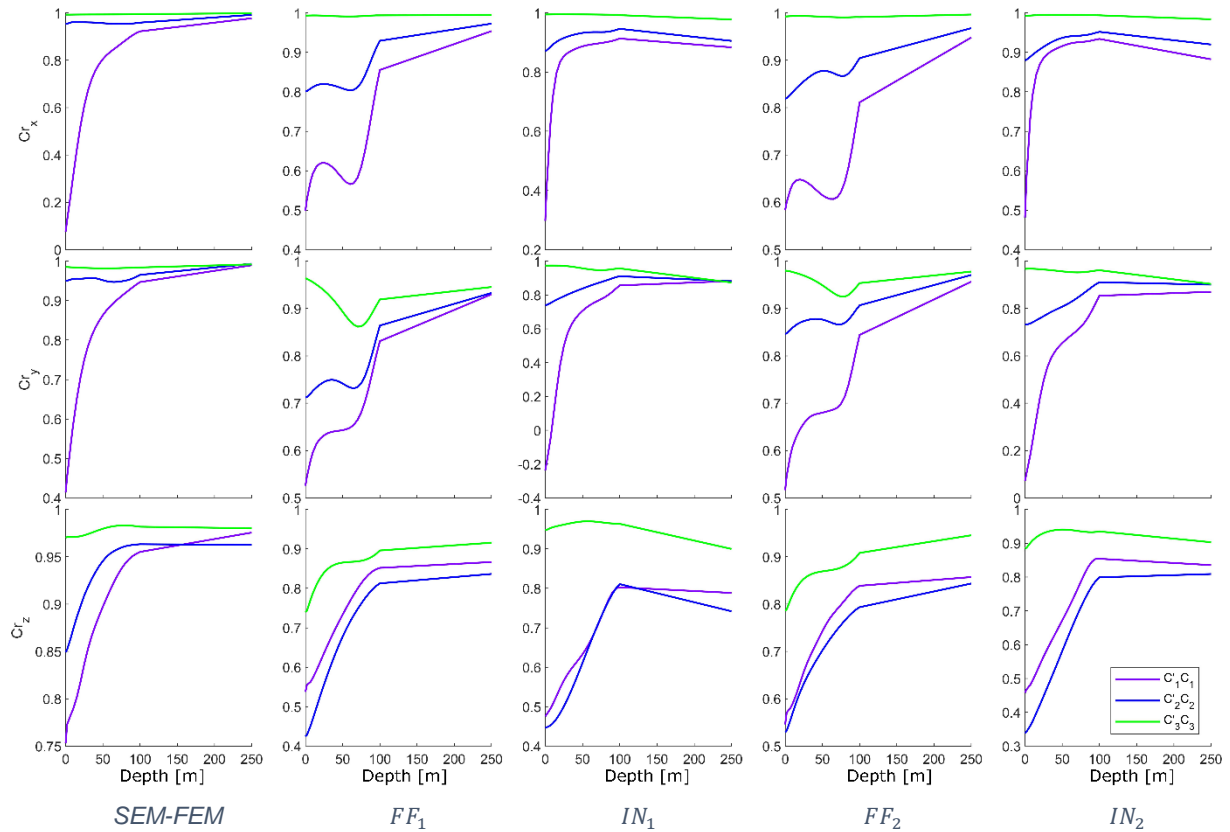
364

365

366

Figure 15 shows a comparison of the recorded accelerations in  $x, y$  and  $z$ -directions, in terms of correlation ( $C_r$  between SSI and FF results, for the soil profiles  $C'_1C_1, C'_2C_2$  and  $C'_3C_3$  (see Appendix B, Figure B-1), for the SEM-FEM coupling and Full FEM analyses considering the input motions  $FF_1, IN_1, FF_2$  and  $IN_2$ . The correlation  $C_r$  is calculated according to the Equation (3) where  $n$  is the number of time steps,  $a_i$  is the corresponding acceleration for the time step index  $i$ ,  $\mu_a$  and  $\sigma_a$  are the mean and standard deviation of the acceleration  $a$ , respectively (Fisher, 1992). This correlation coefficient measures the linear dependence between the acceleration responses in the SSI and FF analysis and quantifies the SSI effect in the soil. A correlation  $C_r = 1$  corresponds to results in the soil unaffected by the presence of the structure.

$$C_r = \frac{1}{n-1} \sum_{i=1}^n \left( \frac{a_{i,FF} - \mu_{a_{FF}}}{\sigma_{a_{FF}}} \right) \left( \frac{a_{i,SSI} - \mu_{a_{SSI}}}{\sigma_{a_{SSI}}} \right) \quad (3)$$



367

368

369

370

Figure 15 Correlation between SSI and FF results along the line profiles  $C_1^1C_1^1$ ,  $C_2^2C_2^2$  and  $C_3^3C_3^3$  for the SEM-FEM coupling and Full FEM analyses considering the input motions  $FF_1, IN_1, FF_2$  and  $IN_2$ .

371

372

373

374

375

376

377

378

379

The results confirm that the domain dimensions considered for the Full FEM SSI calculation, and suggested by Lysmer and Kuhlemeyer (1969), is sufficiently large to satisfy the vertically incident wave and the FF conditions (correlation close to 1 at the base of the model  $z = 250m$  and for  $C_3^3C_3^3$ ). Nevertheless, it is admissible to reduce the domain size to at least 50% for a SEM-FEM SSI analysis coupled by the DRM. On the other hand, results also show the influence of the structure on the soil dynamic response, and hence the soil on the structure, depending on the analysis type and the input motion choice. In fact, for the SEM-FEM analysis, SSI is very important at the ground surface and decreases smoothly with depth. The SSI effect is observed for the Full FEM analysis with IN input motions. However, for the Full FEM analysis with FF input motions, the SSI effect is weaker in the soil and variable with depth.

380

381

382

383

384

385

386

387

388

The dynamic response of the Reactor Pressure Vessel (RPV) structure is examined for SEM-FEM and Full FEM analyses and presented in Figure 16. The comparison between the time history accelerations at different nodes in the structure (Appendix B, Figure B-2) for the SEM-FEM and Full FEM analyses show that the Full FEM analysis results underestimate, in most cases, the response of the structure. A shift of the structure response to lower frequencies is noticed for all Full FEM analyses. The results obtained with IN input motions tends to converge to the SEM-FEM results for higher elevations in structure and present better estimation of the structure response compared to analysis using FF input motions. Finally, the SEM-FEM analysis presents a physic-based solution for SSI analysis considering site effect and variable field input motion. The results show an amplification of the dynamic responses of the soil and the structure due to the additional site effect captured in the SEM-FEM coupling.

389

## 5. CONCLUSIONS AND DISCUSSION

390

391

392

393

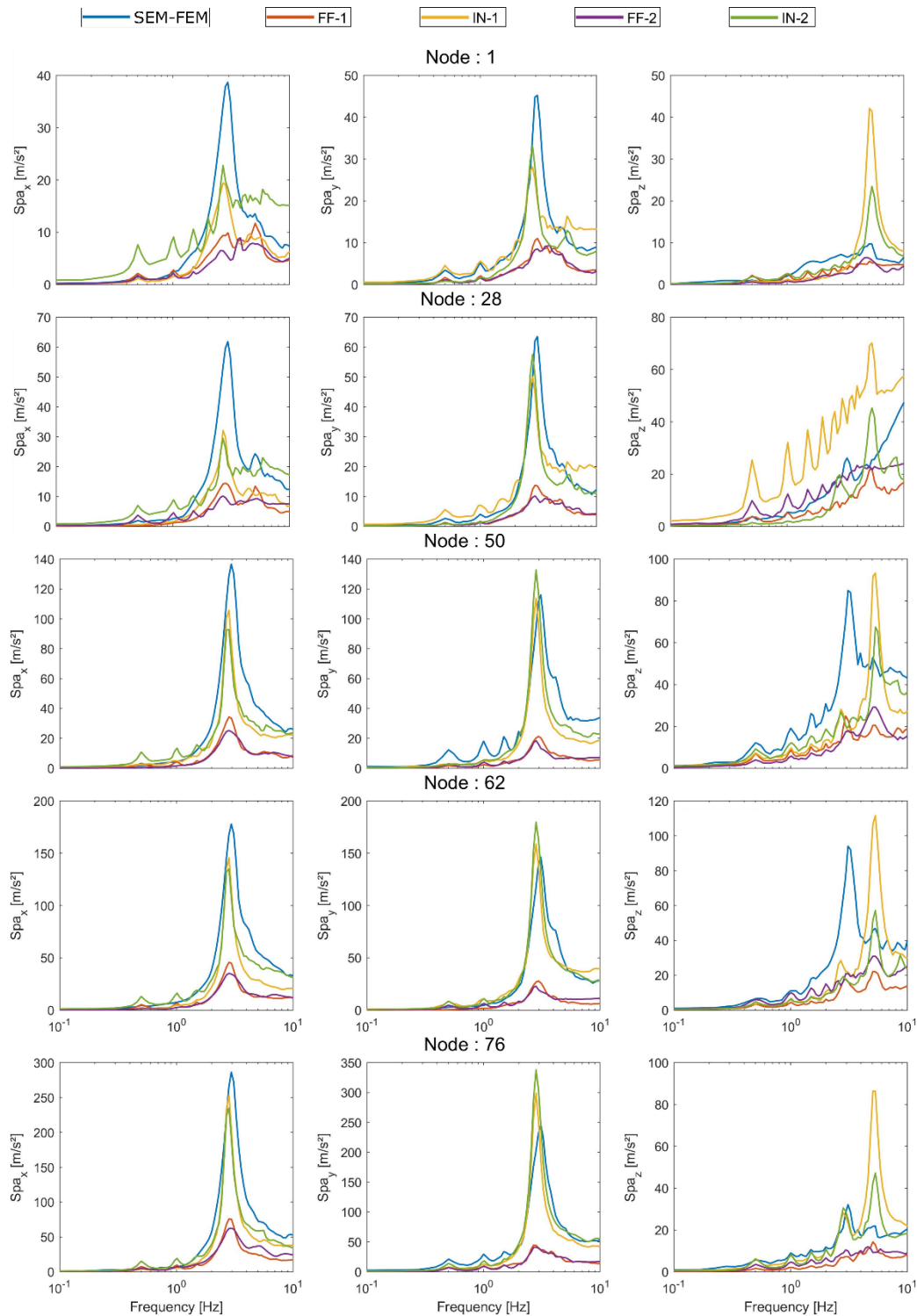
394

395

396

397

In this article, the domain reduction method (DRM) is applied for the coupling between Spectral (SEM) and Finite Element (FEM) Methods, used to solve the wave propagation problem from the fault to the structure. The present study of SEM-FEM coupling leads to a more accurate solution w.r.t the SSI analysis, compared to the case of using a single (full FEM or SEM) method. The coupling method is implemented in Cast3M FEM code (CEA, 2021), and counter-verified using Full FEM (Cast3M) and Full SEM (SEM3D, CEA et al., 2017) analyses. The verification analysis of the coupling using SEM3D and CAST3M codes gives satisfactory results and suggests to use the same time steps and conforming meshes for optimal results. In addition, satisfactory results are obtained for interpolated SEM elements corresponding to the FEM elements.



398

399 *Figure 16 Comparison of the structure response spectra in x, y and z directions in a SSI analysis for the SEM-*  
 400 *FEM coupling and Full FEM analyses considering the input motions FF<sub>1</sub>, IN<sub>1</sub>, FF<sub>2</sub> and IN<sub>2</sub>.*

401 The SEM-FEM coupling is adopted for the Cadarache site, located in the South-Eastern France. The SEM model  
 402 considers the geology complexity of the site including the basin, the fault front and the topography. The FEM  
 403 model considers the near soil, assumed to be horizontally stratified, and the nuclear structure corresponding to a  
 404 simplified virtual PWR type building used for a SSI analysis.

405 A first analysis allows to compare the influence of two methods classically used to define the incident loading  
 406 applied at the boundaries of the near-ground domain: (1) the approach consisting in deconvolving a free field (FF)  
 407 accelerogram recorded at the ground surface of a soil column extracted from the site; (2) the approach consisting  
 408 in convoluting a signal recorded at the base of a soil column (rock or other) also extracted from the site. For this

409 analysis, two FF input motions and two IN (inside bedrock) input motions are considered. The results obtained by  
410 these two approaches show higher accuracy for the deconvolution of the FF input motions regarding the results  
411 obtained in a Full SEM analysis. On the other hand, the results obtained by the convolution of IN input motions  
412 are amplified and can be considered as conservative in an engineering point of view.

413 The four wavefield calculated by the deconvolution of FF and convolution of IN input motions are nevertheless  
414 used here, for the 3D wave propagation in FF and SSI analyses. The results point out the effect of 3D wave  
415 propagation comparing to the 1D deconvolution/convolution approach. Results obtained for a FF analysis with  
416 wavefield calculated from the convolution of IN input motions show more accurate rendering of the frequency  
417 content and amplification comparing to those with wavefields calculated from the convolution of FF input motions.  
418 This result highlights the known differences between 1D and 3D wave propagation analyses. Moreover, the SEM-  
419 FEM analysis shows amplified results compared to all four Full FEM analyses as well as surface waves  
420 propagation. This is due to the additional site effect considering the topography and spatially variable field input  
421 applied at all five surface boundaries in the coupling analysis.

422 The SSI analysis considers a simplified PWR-type building virtually located on the CEA Cadarache site. The  
423 results show that the size of the soil domain to be considered in a SEM-FEM coupling analysis using the DRM  
424 can be reduced by 50% compared to a conventional Full FEM model size recommended by Lysmer and  
425 Kuhlemeyer (1969) to ensure an optimal absorbing boundary condition. A regular dissipation of the SSI effect as  
426 a function of depth and a concentration of these effects near the structure is observed in the cases of SEM-FEM  
427 coupling and Full FEM analyses with the IN input motions. The structure responses are amplified in SEM-FEM  
428 coupling analysis due to the additional site effect captured in this analysis.

429 The DRM method for SSI from the fault to the structure provides a reliable tool for a better understanding of the  
430 response of the structure in its environment. It overcomes the limitation of the SEM to model structural elements  
431 and the Full FEM to model the wave propagation from the fault, with reasonable computation resources. However,  
432 despite the advantages of the coupling some limitations of the coupled codes remains : as the limitation in the  
433 maximum frequency considered in SEM3D or the limitation of Cast3M to model local heterogeneity. On the other  
434 hand, the coupling method is only applicable in the elastic domain as it considers the superposition theorem.  
435 Nonetheless, local nonlinearities of materials can be considered in the reduced FEM domain. Further studies are  
436 necessary to define the applicability of the DRM method considering nonlinear material behavior.

437 Finally, the DRM's SEM-FEM coupling has proved to be a more realistic and physic-based solution for SSI  
438 analysis, taking into account the geometric and mechanical heterogeneities of the site geology in the variable input  
439 force field. However, access to geological data, seismological data, and numerical resources is mandatory for the  
440 coupling analysis and can be pretty challenging.

441

## 442 **ACKNOWLEDGMENTS**

443 This work lies in the framework of the SINAPS@ project funded by the French state and managed by the National  
444 Research Agency under program RNSR Future Investment bearing reference No. ANR-11-RSNR-0022-04. The  
445 SEISM Paris Saclay Research institute has supported the research reported in this paper.

446 Acknowledgments are given to Dr. F. Hollender, project leader, for providing the geological data for the Cadarache  
447 site and Dr F. Wang for the many interesting discussion on the topic.

448

449 **REFERENCES**

- 450 Abell, J.A., Orbović, N., McCallen, D.B., Jeremic, B., 2018. Earthquake soil-structure interaction of nuclear power  
451 plants, differences in response to 3-D,  $3 \times 1$ -D, and 1-D excitations. *Earthq. Eng. Struct. Dyn.* 47, 1478–  
452 1495.
- 453 Anderson, J.G., 2004. Quantitative measure of the goodness-of-fit of synthetic seismograms.
- 454 Baker, J.W., Luco, N., Abrahamson, N.A., Maechling, P.J., Olsen, K.B., 2014. ENGINEERING USES OF  
455 PHYSICS-BASED GROUND MOTION SIMULATIONS. *Stanf. Univ.* 11.
- 456 Baroux, E., Pino, N.A., Valensise, G., Scotti, O., Cushing, M.E., 2003. Source parameters of the 11 June 1909,  
457 Lambesc (Provence, southeastern France) earthquake: A reappraisal based on macroseismic,  
458 seismological, and geodetic observations. *J. Geophys. Res. Solid Earth* 108.  
459 <https://doi.org/10.1029/2002JB002348>
- 460 Berge-Thierry, C., Wang, F., Feau, C., Zentner, I., Voldoire, F., Lopez-Caballero, F., Le Maoult, A., Nicolas, M.,  
461 Ragueneau, F., 2017. The SINAPS@ French Research Project: first lessons of an integrated seismic risk  
462 assessment for nuclear plants safety, in: 16th World Conference on Earthquake, 16WCEE.
- 463 Bielak, J., Loukakis, K., Hisada, Y., Yoshimura, C., 2003. Domain reduction method for three-dimensional  
464 earthquake modeling in localized regions, Part I: Theory. *Bull. Seismol. Soc. Am.* 93, 817–824.
- 465 Boore, D.M., 1972. Finite difference methods for seismic wave propagation in heterogeneous materials. *Methods*  
466 *Comput. Phys.* 11, 1–37.
- 467 Brun, M., De Martin, F., Richart, N., 2021. Hybrid asynchronous SEM/FEM co-simulation for seismic nonlinear  
468 analysis of concrete gravity dams. *Comput. Struct.* 245, 106459.
- 469 Castro-Cruz, D., Gatti, F., Lopez-Caballero, F., 2021. High-fidelity broadband prediction of regional seismic  
470 response: a hybrid coupling of physics-based synthetic simulation and empirical Green functions. *Nat.*  
471 *Hazards* 108, 1997–2031. <https://doi.org/10.1007/s11069-021-04766-x>
- 472 CEA, 2021. Cast3M, <http://www-cast3m.cea.fr/>.
- 473 CEA, CentraleSupélec, IPGP, CNRS, 2017. SEM3D Ver 2017.04 Registered at French Agency for Protection of  
474 Programs (Dépôt APP). French agency for protection of Programs (dépôt APP).
- 475 Clough, R.W., Penzien, J., 2003. Dynamics of structures, Third. ed. Computers & Structures, Berkeley, USA.
- 476 Coleman, J., Jeremic, B., Whittaker, A., 2013. Nonlinear time domain seismic soil structure interaction (SSI)  
477 analysis for nuclear facilities and draft Appendix B of ASCE 4. SMiRT-22 18–23.
- 478 Coleman, J.L., Bolisetti, C., Whittaker, A.S., 2016. Time-domain soil-structure interaction analysis of nuclear  
479 facilities. *Nucl. Eng. Des.* 298, 264–270. <https://doi.org/10.1016/j.nucengdes.2015.08.015>
- 480 Dujardin, A., Hollender, F., Causse, M., Berge-Thierry, C., Delouis, B., Foundotos, L., Ameri, G., Shible, H.,  
481 2020. Optimization of a Simulation Code Coupling Extended Source ( $k=2$ ) and Empirical Green's  
482 Functions: Application to the Case of the Middle Durance Fault. *Pure Appl. Geophys.* 177, 2255–2279.  
483 <https://doi.org/10.1007/s00024-019-02309-x>
- 484 Dupros, F., De Martin, F., Foerster, E., Komatitsch, D., Roman, J., 2010. High-performance finite-element  
485 simulations of seismic wave propagation in three-dimensional nonlinear inelastic geological media.  
486 *Parallel Comput.* 36, 308–325.
- 487 Faccioli, E., Maggio, F., Paolucci, R., Quarteroni, A., 1997. 2D and 3D elastic wave propagation by a pseudo-  
488 spectral domain decomposition method. *J. Seismol.* 1, 237–251.
- 489 Fares, R., 2018. Techniques de modélisation pour la conception des bâtiments parasismiques en tenant compte de  
490 l'interaction sol-structure (thesis). Côte d'Azur.
- 491 Fares, R., Santisi d'Avila, M.P., Deschamps, A., 2019. Soil-structure interaction analysis using a 1DT-3C wave  
492 propagation model. *Soil Dyn. Earthq. Eng.* 120, 200–213. <https://doi.org/10.1016/j.soildyn.2019.02.011>
- 493 Festa, G., Vilotte, J.-P., 2005. The Newmark scheme as velocity–stress time-staggering: an efficient PML  
494 implementation for spectral element simulations of elastodynamics. *Geophys. J. Int.* 161, 789–812.
- 495 Fisher, R.A., 1992. Statistical Methods for Research Workers, in: Kotz, S., Johnson, N.L. (Eds.), Breakthroughs  
496 in Statistics: Methodology and Distribution, Springer Series in Statistics. Springer, New York, NY, pp.  
497 66–70. [https://doi.org/10.1007/978-1-4612-4380-9\\_6](https://doi.org/10.1007/978-1-4612-4380-9_6)
- 498 Gatti, F., 2017. Analyse physics-based de scénarios sismiques «de la faille au site»: prédiction de mouvement  
499 sismique fort pour l'étude de vulnérabilité sismique de structures critiques. (phdthesis). Université Paris-  
500 Saclay ; Politecnico di Milano.
- 501 Gatti, F., Lopez-Caballero, F., Paolucci, R., Clouteau, D., 2018. Near-source effects and non-linear site response  
502 at Kashiwazaki-Kariwa Nuclear Power Plant, in the 2007 Chuetsu-Oki earthquake: evidence from surface  
503 and downhole records and 1D numerical simulations. *Bull. Earthq. Eng.* 16, 1105–1135.  
504 <https://doi.org/10.1007/s10518-017-0255-y>
- 505 Guidotti, R., Mazzieri, I., Stupazzini, M., Dagna, P., 2012. 3D numerical simulation of the site-city interaction  
506 during the 22 February 2011 MW 6.2 Christchurch earthquake, in: 15th World Conference of Earthquake  
507 Engineering.



- 508 Gupta, O., Lacoste, A.C., 2006. Prise en compte du risque sismique à la conception des ouvrages de génie civil  
509 d'installations nucléaire de base à l'exception des stockages à long terme des déchets radioactifs. Guide  
510 de l'Autorité de Sûreté Nucléaire. Guide L'Autorité Sûreté Nucl.
- 511 Guyonnet-Benaize, C., 2011. Modélisation 3D multi-échelle des structures géologiques de la région de la faille de  
512 la moyenne Durance (SE France). Aix-Marseille 1.
- 513 Hudson, M., Idriss, I.M., Beikae, M., 1994. QUAD4M: a computer program to evaluate the seismic response of  
514 soil structures using finite element procedures and incorporating a compliant base. Center for  
515 Geotechnical Modeling, Department of Civil and Environmental ....
- 516 Hughes, T.J.R., 1987. The finite element method - linear static and dynamic finite element analysis. Prentice Hall  
517 Englewood Cliff 490–567.
- 518 IAEA, I.A.E.A., 2011. Guidance Document - PART 1: K-K Unit 7 R/B Structure, PHASE I, II & III (No. IAEA-  
519 EBP-SS-WA2-KARISMA-SP-002). Vienna.
- 520 IAEA, I.A.E.A., 2009. General specification for the KARISMA Benchmark Exercise (No. IAEA-EBP-SS-WA2-  
521 KARISMA-SP-0012009). Vienna.
- 522 Ichimura, T., Fujita, K., Tanaka, S., Hori, M., Lalith, M., Shizawa, Y., Kobayashi, H., 2014. Physics-Based Urban  
523 Earthquake Simulation Enhanced by 10.7 BlnDOF × 30 K Time-Step Unstructured FE Non-Linear  
524 Seismic Wave Simulation, in: SC '14: Proceedings of the International Conference for High Performance  
525 Computing, Networking, Storage and Analysis. Presented at the SC '14: Proceedings of the International  
526 Conference for High Performance Computing, Networking, Storage and Analysis, pp. 15–26.  
527 <https://doi.org/10.1109/SC.2014.7>
- 528 Imperatori, W., Mai, P.M., 2015. The role of topography and lateral velocity heterogeneities on near-source  
529 scattering and ground-motion variability. *Geophys. J. Int.* 202, 2163–2181.
- 530 Jeremic, B., Jie, G., Preisig, M., Tafazzoli, N., 2009. Time domain simulation of soil–foundation–structure  
531 interaction in non-uniform soils. *Earthq. Eng. Struct. Dyn.* 38, 699–718.
- 532 Komatitsch, D., Vilotte, J.-P., 1998. The spectral element method: An efficient tool to simulate the seismic  
533 response of 2D and 3D geological structures. *Bull. Seismol. Soc. Am.* 88, 368–392.
- 534 Korres, M., Lopez-Caballero, F., Alves Fernandes, V., Gatti, F., Zentner, I., Voldoire, F., Clouteau, D., Castro-  
535 Cruz, D., 2022. Enhanced Seismic Response Prediction of Critical Structures via 3D Regional Scale  
536 Physics-Based Earthquake Simulation. *J. Earthq. Eng.* 1–29.
- 537 Koufoudi, E., Cornou, C., Grange, S., Dufour, F., Imtiaz, A., 2015. Quantification of the spatially variable ground  
538 motion and its influence on the linear and non-linear structural response of a single degree of freedom.  
539 Application to the shallow sedimentary valley of Argostoli, Greece.
- 540 Lo Frano, R., Pugliese, G., Forasassi, G., 2010. Preliminary seismic analysis of an innovative near term reactor:  
541 Methodology and application. *Nucl. Eng. Des.* 240, 1671–1678.  
542 <https://doi.org/10.1016/j.nucengdes.2010.02.034>
- 543 Lu, X., Tian, Y., Wang, G., Huang, D., 2018. A numerical coupling scheme for nonlinear time history analysis of  
544 buildings on a regional scale considering site-city interaction effects. *Earthq. Eng. Struct. Dyn.* 47, 2708–  
545 2725. <https://doi.org/10.1002/eqe.3108>
- 546 Luo, C., Lou, M., Gui, G., Wang, H., 2019. A modified domain reduction method for numerical simulation of  
547 wave propagation in localized regions. *Earthq. Eng. Vib.* 18, 35–52.
- 548 Lysmer, J., Kuhlemeyer, R.L., 1969. Finite dynamic model for infinite media. *J. Eng. Mech. Div.* 95, 859–878.
- 549 Lysmer, J., Udaka, T., Tsai, C., Seed, H.B., 1975. Flush - a Computer Program for Approximate 3-D Analysis of  
550 Soil-Structure Interaction Problems (No. PB-259332; EERC-75-30). California Univ., Richmond (USA).  
551 Earthquake Engineering Research Center.
- 552 Maeda, T., Takemura, S., Furumura, T., 2017. OpenSWPC: an open-source integrated parallel simulation code for  
553 modeling seismic wave propagation in 3D heterogeneous viscoelastic media. *Earth Planets Space* 69, 1–  
554 20.
- 555 Manakou, M.V., Raptakis, D.G., Chávez-García, F.J., Apostolidis, P.I., Ptilakis, K.D., 2010. 3D soil structure of  
556 the Mygdonian basin for site response analysis. *Soil Dyn. Earthq. Eng.* 30, 1198–1211.  
557 <https://doi.org/10.1016/j.soildyn.2010.04.027>
- 558 McCallen, D., Petersson, A., Rodgers, A., Pitarka, A., Miah, M., Petrone, F., Sjogreen, B., Abrahamson, N., Tang,  
559 H., 2020. EQSIM—A multidisciplinary framework for fault-to-structure earthquake simulations on  
560 exascale computers part I: Computational models and workflow. *Earthq. Spectra* 8755293020970982.  
561 <https://doi.org/10.1177/8755293020970982>
- 562 McCallen, D., Petrone, F., Miah, M., Pitarka, A., Rodgers, A., Abrahamson, N., 2021. EQSIM—A  
563 multidisciplinary framework for fault-to-structure earthquake simulations on exascale computers, part II:  
564 Regional simulations of building response. *Earthq. Spectra* 37, 736–761.
- 565 Mercerat, E.D., Vilotte, J.P., Sánchez-Sesma, F.J., 2006. Triangular Spectral Element simulation of two-  
566 dimensional elastic wave propagation using unstructured triangular grids. *Geophys. J. Int.* 166, 679–698.  
567 <https://doi.org/10.1111/j.1365-246X.2006.03006.x>

- 568 Moczo, P., Kristek, J., Halada, L., 2004. The finite-difference method for seismologists. *Introd. Comenius Univ.*  
569 Bratisl.
- 570 Perron, V., Gélis, C., Froment, B., Hollender, F., Bard, P.-Y., Cultrera, G., Cushing, E.M., 2018. Can broad-band  
571 earthquake site responses be predicted by the ambient noise spectral ratio? Insight from observations at  
572 two sedimentary basins. *Geophys. J. Int.* 215, 1442–1454. <https://doi.org/10.1093/gji/ggy355>
- 573 Raptakis, D., Chávez-García, F.J., Makra, K., Ptilakis, K., 2000. Site effects at Euroseistest—I. Determination of  
574 the valley structure and confrontation of observations with 1D analysis. *Soil Dyn. Earthq. Eng.* 19, 1–22.  
575 [https://doi.org/10.1016/S0267-7261\(99\)00025-1](https://doi.org/10.1016/S0267-7261(99)00025-1)
- 576 Régnier, J., Bonilla, L.-F., Bard, P.-Y., Bertrand, E., Hollender, F., Kawase, H., Sicilia, D., Arduino, P., Amorosi,  
577 A., Asimaki, D., Boldini, D., Chen, L., Chiaradonna, A., DeMartin, F., Ebrille, M., Elgamal, A., Falcone,  
578 G., Foerster, E., Foti, S., Garini, E., Gazetas, G., Gélis, C., Ghofrani, A., Giannakou, A., Gingery, J.R.,  
579 Glnisky, N., Harmon, J., Hashash, Y., Iai, S., Jeremić, B., Kramer, S., Kontoe, S., Kristek, J., Lanzo, G.,  
580 Lernia, A. di, Lopez-Caballero, F., Marot, M., McAllister, G., Mercerat, E.D., Moczo, P., Montoya-  
581 Noguera, S., Musgrove, M., Nieto-Ferro, A., Pagliaroli, A., Pisanò, F., Richterova, A., Sajana, S., d’Avila,  
582 M.P.S., Shi, J., Silvestri, F., Taiebat, M., Tropeano, G., Verrucci, L., Watanabe, K., 2016. International  
583 benchmark on numerical simulations for 1D, nonlinear site response (PRENOLIN): Verification phase  
584 based on canonical cases. *Bull. Seismol. Soc. Am.* 106, 2112–2135. <https://doi.org/10.1785/0120150284>
- 585 Russo, A.D., Sica, S., Del Gaudio, S., De Matteis, R., Zollo, A., 2017. Near-source effects on the ground motion  
586 occurred at the Conza Dam site (Italy) during the 1980 Irpinia earthquake. *Bull. Earthq. Eng.* 15, 4009–  
587 4037.
- 588 Saez, E., Lopez Caballero, F., Modaressi-Farahmand-Razavi, A., 2011. Effect of the inelastic dynamic soil–  
589 structure interaction on the seismic vulnerability assessment. *Struct. Saf.* 33, 51–63.  
590 <https://doi.org/10.1016/j.strusafe.2010.05.004>
- 591 Santisi d’Avila, M.P., Lenti, L., 2012. Modeling strong seismic ground motion: 3D loading path vs wavefield  
592 polarization. *Geophys. J. Int.*
- 593 Santisi d’Avila, M.P., Lenti, L., Gobbi, S., Fares, R., 2022. Reduced T-shaped soil domain for nonlinear dynamic  
594 soil-bridge interaction analysis. *Adv. Bridge Eng.* 3, 9. <https://doi.org/10.1186/s43251-022-00057-y>
- 595 Schwer, L.E., 2009. Guide for verification and validation in computational solid mechanics.
- 596 Semblat, J.-F., 1997. Rheological Interpretation of Rayleigh Damping. *J. Sound Vib.* 206, 741–744.  
597 <https://doi.org/10.1006/jsvi.1997.1067>
- 598 Semblat, J.F., Kham, M., Parara, E., Bard, P.Y., Ptilakis, K., Makra, K., Raptakis, D., 2005. Seismic wave  
599 amplification: Basin geometry vs soil layering. *Soil Dyn. Earthq. Eng.*, 11th International Conference on  
600 Soil Dynamics and Earthquake Engineering (ICSDEE): Part 1 25, 529–538.  
601 <https://doi.org/10.1016/j.soildyn.2004.11.003>
- 602 Sextos, A.G., Kappos, A.J., 2008. Evaluation of seismic response of bridges under asynchronous excitation and  
603 comparisons with Eurocode 8-2 provisions. *Bull. Earthq. Eng.* 7, 519. [https://doi.org/10.1007/s10518-](https://doi.org/10.1007/s10518-008-9090-5)  
604 008-9090-5
- 605 Takemura, S., Furumura, T., Maeda, T., 2015. Scattering of high-frequency seismic waves caused by irregular  
606 surface topography and small-scale velocity inhomogeneity. *Geophys. J. Int.* 201, 459–474.
- 607 Touhami, S., Gatti, F., Lopez-Caballero, F., Cottureau, R., de Abreu Corrêa, L., Aubry, L., Clouteau, D., 2022.  
608 SEM3D: A 3D High-Fidelity Numerical Earthquake Simulator for Broadband (0–10 Hz) Seismic  
609 Response Prediction at a Regional Scale. *Geosciences* 12, 112.  
610 <https://doi.org/10.3390/geosciences12030112>
- 611 Van Nguyen, D., Kim, D., Duy Nguyen, D., 2020. Nonlinear seismic soil-structure interaction analysis of nuclear  
612 reactor building considering the effect of earthquake frequency content. *Structures* 26, 901–914.  
613 <https://doi.org/10.1016/j.istruc.2020.05.013>
- 614 Virieux, J., 1986. P-SV wave propagation in heterogeneous media: Velocity-stress finite-difference method.  
615 *Geophysics* 51, 889–901.
- 616 Wang, F., Feau, C., 2017. Seismic fragility curve estimation using signals generated with GMPE-Case study on  
617 the Kashiwazaki-kariwa power plant, in: SMiRT 24, Structural Mechanics in Reactor Technology.  
618 International Association for Structural Mechanics in Reactor Technology.
- 619 Wang, F., Rambach, M., 2013. Contribution to the IAEA soil-structure interaction KARISMA Benchmark.
- 620 Wang, H., Yang, H., Feng, Y., Jeremić, B., 2021. Modeling and simulation of earthquake soil structure interaction  
621 excited by inclined seismic waves. *Soil Dyn. Earthq. Eng.* 146, 106720.
- 622 Zhang, L., Wang, J.-T., Xu, Y.-J., He, C.-H., Zhang, C.-H., 2020. A Procedure for 3D Seismic Simulation from  
623 Rupture to Structures by Coupling SEM and FEM. *Bull. Seismol. Soc. Am.* 110, 1134–1148.
- 624 Zuchowski, L., Brun, M., De Martin, F., 2018. Co-simulation coupling spectral/finite elements for 3D  
625 soil/structure interaction problems. *Comptes Rendus Mécanique* 346, 408–422.
- 626

628 **APPENDIX A**629 *Tableau A-1 Mechanical properties of the structure*

Module de Young $E[GP\grave{a}]$	Densité $\rho[Kg/m^3]$	Coef. d'amortissement $\xi$	Coef. de Poisson $\nu$
36	5000	0.07	0.2

630

631 *Tableau A-2 Velocity and density model of the Cadarache site basin*

$z[m]$	$v_s(z)[m/s]$	$v_p(z)[m/s]$	$\rho(z)[kg/m^3]$
$0 \leq z \leftarrow 7m$	$400 + 130z^{0.5}$	900	2100
$z \leq -7m$	$400 + 130z^{0.5}$	$1500 + 190z^{0.5}$	2100

632

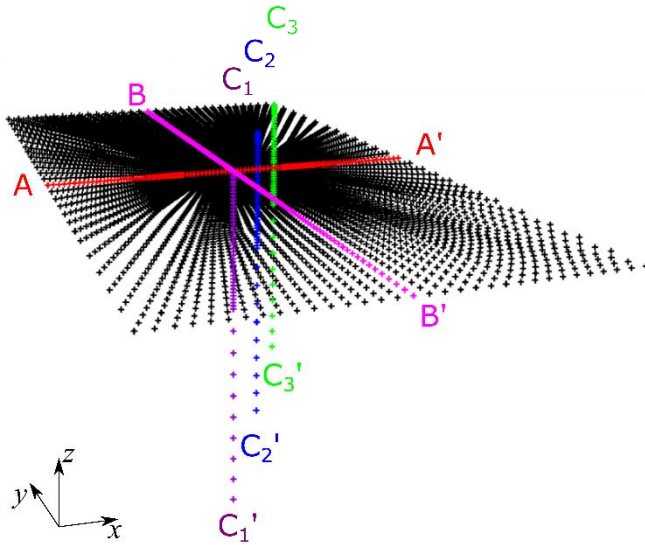
633 *Tableau A-3 Velocity and density model of the Cadarache bedrock*

$z[m]$	$v_s(z)[m/s]$	$v_p(z)[m/s]$	$\rho(z)[kg/m^3]$
$0 \leq z \leftarrow 60m$	$1000 + 427z^{0.4}$	$2000 + 1054z^{0.3}$	2500
$-60 \leq z \leftarrow 3000m$	3200	5600	2720

634

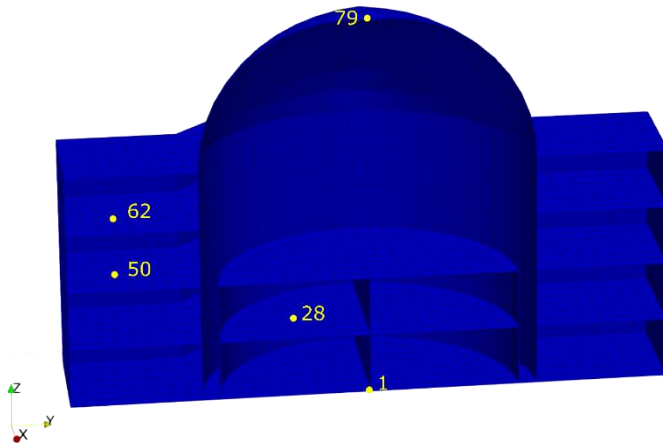
635 *Tableau A-4 Mechanical characteristics of the FEM soil profile model*

$n^\circ$	$z[m]$	$h[m]$	$v_s(z)[m/s]$	$v_p(z)[m/s]$	$\rho(z)[kg/m^3]$	$\nu$
1	2	2	583.848	900	2100	0.13668
2	7	5	743.948	2002.69	2100	0.41996
3	10	3	811.096	2100.83	2100	0.41241
4	15	5	903.488	2235.87	2100	0.40242
5	20	5	981.378	2349.71	2100	0.39435
6	25	5	1050	2450	2100	0.3875
7	30	5	1112.04	2540.67	2100	0.38151
8	35	5	1169.09	2624.06	2100	0.37617
9	40	5	1222.19	2701.67	2100	0.37134
10	45	5	1272.07	2774.56	2100	0.36693
11	50	5	1319.24	2843.5	2100	0.36286
12	55	5	1364.11	2909.08	2100	0.35907
13	60	5	1406.98	2971.73	2100	0.35554
14	65	5	1448.09	3031.83	2100	0.35222
15	70	5	1487.66	3089.65	2100	0.34909
16	75	5	1525.83	3145.45	2100	0.34614
17	80	5	1562.76	3199.41	2100	0.34333
18	85	5	1598.54	3251.71	2100	0.34066
19	90	5	1633.29	3302.5	2100	0.33811
20	95	5	1667.08	3351.89	2100	0.33567
21	100	5	1700	3400	2100	0.33333
22	250	150	3200	5600	2720	0.25758



637  
 638 *Figure B-1 Nodes lines, in the soil model, along which the results history output are evaluated*

639



640  
 641 *Figure B-2 Nodes in the structure model along which the results history outputs are evaluated*

642 *Table B-1 Coordinates of the observed structure nodes*

Node #	x	y	z
1	0.0	0.0	0.0
28	10	-12	10.0
50	12	-39	20.0
62	12	-39	30.0
79	0.0	0.0	65

643